Materials Advances

ROYAL SOCIETY OF CHEMISTRY

PAPER

View Article Online
View Journal

Cite this: DOI: 10.1039/d6ma00481d

On the magnetocaloric effect in biphasic FeCrSiB amorphous composites

Alba Sanz-Prada,[ab] Javier López-García,*[ac] Kenny Padrón-Alemán,[ab] Jose M. Porro,[de] José L. Sánchez Llamazares,[f] Jesús A. Blanco,[a] Pedro Gorria*[ac] and Pablo Álvarez-Alonso[ac]

Received 6th April 2026,
Accepted 2nd June 2026

DOI: 10.1039/d6ma00481d

rsc.li/materials-advances

Room-temperature magnetic refrigeration using the Ericsson cycle relies on materials with a large, nearly constant magnetocaloric (MC) effect over a wide temperature range. Here, we examine the MC properties of biphasic composite systems made from Fe–Cr–Si–B amorphous alloys. The precursor compositions, $Fe_{68.8}Cr_{11.2}Si_6B_{14}$ and $Fe_{70.4}Cr_{9.6}Si_6B_{14}$, show a second-order magnetic phase transition with values of the Curie temperature (T_C) of 290 K and 340 K, respectively. Analysis of critical exponents reveals that both alloys display intermediate critical behavior, between mean-field and three-dimensional Heisenberg universality classes. Guided by the individual isothermal magnetic entropy change *versus* temperature curves [$\Delta S(T)$], we have designed a composite by combining the two alloys in proportions that yield a nearly constant $|\Delta S_{comp}|$, achieving a value $\approx$1.7 J kg^{-1} K^{-1} for a magnetic field change of $\mu_0\Delta H$ = 5 T. This table-like behavior persists over a temperature range of about 50 K, as determined by the T_C values of the parent alloys. We also assessed the effective refrigerant capacity (RC_{eff}) and temperature-averaged entropy change (TEC) for the composite. The customized MC response delivers a competitive RC_{eff} (87 J kg^{-1} at $\mu_0\Delta H$ = 5 T) and a TEC that is almost independent of the operating temperature range. This shows that rational design of Fe-based amorphous composites provides an adaptable solution for Ericsson-cycle magnetic refrigeration by balancing performance, operating temperature, and material cost.

Introduction

Metallic amorphous materials, or metallic glasses, are solids lacking long-range atomic order, meaning that the atomic positions do not follow a periodic pattern like in crystalline materials. This structural disorder greatly influences physical properties. Most of ferromagnetic metallic glasses exhibit isotropic magnetic behavior, mainly due to the absence of magnetocrystalline anisotropy (directional dependence of magnetic properties in crystals) and grain-boundary effects (coming from the interfaces between different crystalline regions). This usually leads to reduced hysteresis losses (less energy loss during magnetic cycling), enhanced corrosion resistance, and improved mechanical resilience.[1] These features have made amorphous metallic alloys key functional materials in soft magnetic technologies and, more recently, in energy-related applications.[2]

Moreover, metallic glasses have attracted particular attention for solid-state refrigeration *via* the magnetocaloric effect (MCE),[3] which refers to the heating or cooling of a material when it is exposed to a change in magnetic field. Magnetic refrigeration is a sustainable alternative to vapor-compression cooling, offering higher efficiency and eliminating the use of greenhouse refrigerant gases.[4] The MCE originates from the isothermal magnetic entropy change (ΔS) associated with field-induced spin ordering and depends sensitively on magnetic exchange interactions and thermodynamic response.

The conventional magnetocaloric (MC) materials with promising functionality are primarily crystalline rare-earth intermetallics and compounds exhibiting a first-order magnetostructural phase transition (FOPT). These materials frequently exhibit substantial ΔS values, but they also present drawbacks such as thermal and magnetic hysteresis, mechanical brittleness, and limited cycling stability.[5] In contrast, metallic glasses usually exhibit second-order magnetic phase transitions (SOMPT) with

[a] Departamento de Física, Universidad de Oviedo, C/Calvo Sotelo, 18, Oviedo 33007, Spain. E-mail: lopezjavier@uniovi.es, pgorria@uniovi.es
[b] Institut Laue-Langevin, 71 Avenue des Martyrs, CS20156, Grenoble 38042 Cédex 9, France
[c] IUTA, Universidad de Oviedo, Gijón 33203, Spain
[d] BCMaterials, Basque Center for Materials, Applications & Nanostructures, Leioa 48940, Spain
[e] Ikerbasque, Basque Foundation for Science, Bilbao 48009, Spain
[f] Instituto Potosino de Investigación Científica y Tecnológica A.C., Camino a la Presa San José 2055, 78216, San Luis Potosí, Mexico

negligible hysteresis favored by the as-mentioned lack of long-range structural coupling.[5] Their MCE is frequently lower than that of FOPT materials. However, their broad magnetic transitions, excellent soft magnetic properties, mechanical stability, and compositional tunability can yield competitive refrigerant capacities and reliable operation features.[6]

Among amorphous MC systems, rare-earth- and transition-metal-based alloys constitute the two main families.[7] Rare-earth-based glasses can display large MCE values, but their Curie temperature (T_C) values are habitually confined to the cryogenic regime, limiting their application to magnetic refrigeration for gas liquefaction.[7] However, Fe-based amorphous alloys represent a versatile alternative for room temperature (RT) refrigeration. They combine second-order transitions with a T_C close to RT and low raw material cost.[6] These characteristics make them particularly attractive for near-RT magnetic refrigeration.[8–10] Nevertheless, despite the favorable properties exhibited by second-order materials, they rarely display the ''table-like'' entropy change profile (*i.e.*, almost constant temperature-dependence of ΔS) required for an Ericsson-type refrigeration cycle.[11]

One well-established and effective strategy to overcome this limitation is to design composite materials that combine phases with slightly different values of their T_C to extend and flatten the $\Delta S(T)$ curve.[12–18] Fe-based amorphous alloys are especially suitable as parent phases for such composites, thanks to their large thermal stability (with crystallization temperatures typically above 750 K[19–21]) and their relatively low cost compared with the rare-earth-based metallic glasses. In particular, interest in Fe–Cr–Si–B amorphous alloys has recently increased, both from a fundamental perspective focused on magnetic relaxation processes and crystallization kinetics,[22] and also for MC applications.[23–25]

In this work, we investigate the MC response of Fe–Cr–Si–B melt-spun ribbons with Curie temperatures close to room temperature and their composites. In particular, we have selected $Fe_{70.4}Cr_{9.6}Si_6B_{14}$ and $Fe_{68.8}Cr_{11.2}Si_6B_{14}$ ribbons from our previous systematic study in the $(Fe_{1-x}Cr_x)_{80}Si_6B_{14}$ system,[25] given that their T_C separation of approximately 50 K is particularly suitable for designing a composite with an almost flat isothermal magnetic entropy change. Particular emphasis is placed on the functional design of a broad table-like $\Delta S(T)$ response for Ericsson-cycle refrigeration, the magnetic-field dependence of the composite magnetocaloric behavior, and its impact on application-relevant figures of merit such as the effective refrigerant capacity (RC_{eff}) and the temperature-averaged entropy change (TEC). Furthermore, through critical exponent analysis, we establish a direct correlation between scaling behavior and the extended $\Delta S(T)$ curves observed in these amorphous systems. Our results demonstrate that rare-earth-free Fe-based amorphous composites can achieve competitive MC performance while combining low magnetic losses, scalability, and cost-effective processing, making them promising candidates for RT magnetic cooling.

Experimental methods and numerical calculations

Two amorphous ribbons, 25 μm thick and 1 mm wide, with nominal compositions $Fe_{70.4}Cr_{9.6}Si_6B_{14}$ (ribbon A) and $Fe_{68.8}Cr_{11.2}Si_6B_{14}$ (ribbon B) were fabricated by melt-spinning as described elsewhere.[25] X-ray diffraction (XRD) analysis was performed in a high-resolution Rigaku Smartlab diffractometer with Cu-Kα_1 radiation to evaluate the amorphous nature of the samples. Fig. S1 depicts the XRD patterns of both samples. The absence of any sharp Bragg reflections, and the appearance of the characteristic broad halo of amorphous materials evidence the lack of long range crystalline order.

Isothermal magnetization curves, $M(\mu_0 H)$, as well as magnetization *vs.* temperature curves, $M(T)$, were collected under applied magnetic field values up to 8 T in the 150–400 K range using a Quantum Design PPMS EverCool-9T system equipped with a vibrating sample magnetometer (VSM). The ribbon length was aligned with the direction of the magnetic field to minimize demagnetizing-field effects. The isothermal $\Delta S(T)$ curves were determined by numerically integrating a set of isothermal $M(\mu_0 H)$ curves using the Maxwell relation:[26]

$$\Delta S(T, \mu_0 H) = \int_0^{\mu_0 H} \left(\frac{\partial M}{\partial T}\right)_H \mathrm{d}H \quad (1)$$

The magnetic and magnetocaloric measurements were performed on multiple pieces cut from the same melt-spun ribbons, ensuring representative sampling of each composition. The reported data reflect consistent behavior across these pieces, indicating good batch homogeneity typical of rapidly quenched Fe-based amorphous alloys.

For each value of the applied magnetic field the isothermal magnetic entropy change of the composite was calculated as:[27]

$$\Delta S_{comp}(T) = \alpha \cdot \Delta S_A(T) + (1 - \alpha) \cdot \Delta S_B(T) \quad (2)$$

where, $\Delta S_A(T)$ and $\Delta S_B(T)$ refer to the isothermal magnetic entropy change measured for each individual ribbon, while the symbol α denotes the weight fraction (mass proportion) of the A-type ribbons.

Results and discussion

Magnetic behavior of individual alloys

The inset in Fig. 1 shows the $M(T)$ curves (normalized to the value at T = 150 K) for ribbons A and B under a low 5 mT applied magnetic field. Magnetization decreases gradually with temperature, vanishing at the second-order ferromagnetic (FM) to paramagnetic (PM) phase transition ($T = T_C$). Further support for the ferromagnetic character of the samples is provided by the hysteresis loop (depicted in Fig. S2), which exhibits a characteristic low coercive field of 19 A m^{-1} (0.24 Oe). There is not any evidence of secondary magnetic phases in the $M(T)$ data within the measured temperature range. The values of the Curie temperature, estimated from the minima of the dM/dT *versus* T curves (not shown), are T_C^A = 340(2) K for ribbon A and

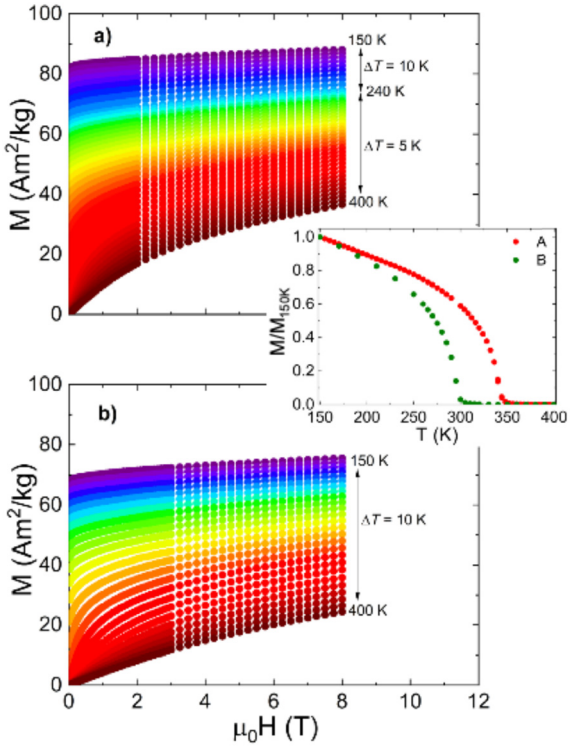

Fig. 1 Isothermal magnetization curves, $M(\mu_0 H)$, measured at temperatures ranging from 150 to 400 K in steps of 5 and 10 K for (a) ribbons A, and (b) ribbons B. Inset: Temperature dependence of the reduced magnetization $M/M_{150\,K}$, where $M_{150\,K}$ is the magnetization measured at 150 K under an applied magnetic field of 5 mT. The inflection point of the curve provides an estimate of the Curie temperatures of both samples (see the text).

T_C^B = 290(2) K for ribbon B.[25] These values fall within the temperature range relevant for household magnetic refrigeration, including RT cooling and air-conditioning. The difference in T_C between the two compositions is attributed to variations in the Fe–Fe exchange interactions, which are influenced by the Cr content and the local atomic environment.[28]

Isothermal magnetization curves measured over the temperature interval 150–400 K for both ribbons are shown in Fig. 1. In all cases, magnetization increases rapidly in the low magnetic field region, thus indicating a low magnetic anisotropy.

Under higher values of the applied magnetic field, the $M(\mu_0 H)$ curves exhibit a tendency toward saturation; however, full saturation is not achieved at temperatures close to T_C even for $\mu_0 H$ = 8 T. Therefore, a fit of the $M(\mu_0 H)$ curves to a classical approach-to-saturation law was used to estimate the value of saturation magnetization (M_S) at zero magnetic field:

$$M = M_S\left(1 - \frac{a}{H^2}\right) + \chi_0 H \qquad (3)$$

where a is a coefficient related to magnetic hardness and χ_0 is the field-independent magnetic susceptibility.[29] As shown in Fig. S3, the resulting $M_S(T)$ values for ribbon B are consistently lower than those of ribbon A. There are two main reasons for this observation: the reduced T_C^B, due to the enhancement of the antiferromagnetic Fe–Cr exchange coupling with increasing Cr content,[28] and the reduced Fe content of the B ribbon.

The concavity of the Arrott's plots evolves progressively with increasing temperature, as shown in Fig. S4, changing from convex to concave behavior. According to Banerjee's criterion,[30] this evolution is characteristic of an FM–PM SOMPT. Moreover, T_C can be estimated by extrapolating the high-magnetic field linear region of each isotherm toward the zero-field region; the isotherm whose extrapolation passes through the origin corresponds to T_C.[31] For ribbons A and B, these estimated values are approximately 370 K and 330 K, respectively, higher than those estimated from the minimum in the dM/dT *vs.* T curves.

Furthermore, the convex curvature persists even at temperatures above T_C. These observations suggest that the conventional analysis of the Arrott's plots is inadequate to accurately describe the critical behavior of this system. Therefore, modified Arrott plots (MAPs), which incorporate the critical exponents β and γ, should be used to determine the magnetic transition parameters more reliably [see Fig. 2 for $M^{1/\beta}$ *vs.* $(\mu_0 H/M)^{1/\gamma}$ plots].[32] By means of the Kouvel–Fisher (KF) method,[33] the critical exponents β = 0.423(5), γ = 1.6(1), and δ = 4.8(3) (δ values were derived from the Widom relation,[34] $\delta = 1 + \gamma/\beta$) were estimated for ribbon A. For ribbon B, β = 0.423(3),

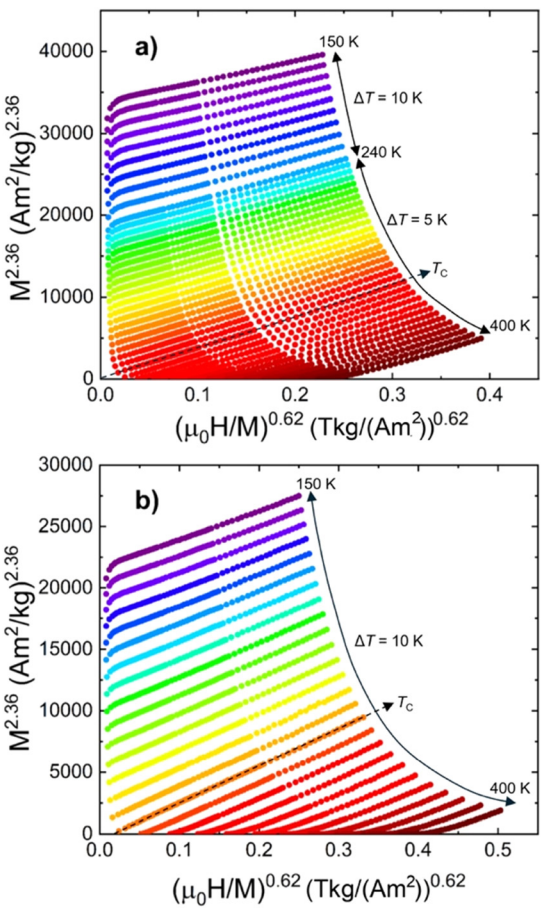

Fig. 2 Modified Arrott plots ($M^{1/\beta}$ *vs.* $(\mu_0 H/M)^{1/\gamma}$) measured between 150 K and 400 K for (a) ribbons A, and (b) ribbons B. The critical exponents β and γ were determined from the Kouvel–Fisher method (see below).

γ = 1.62(2), and δ = 4.83(7) were obtained. These critical exponents differ from those expected in the mean-field (MF) model (*i.e.*, β = 0.5, γ = 1.0, δ = 3.0).[35] In fact, the experimental value of the exponent β lies between those of the MF and 3D-Heisenberg predictions (β = 0.365).[35] This finding points to a magnetic regime governed by the coexistence of long-range interactions, typical of MF behavior, and short-range correlations consistent with a 3D-Heisenberg model.[36,37]

However, the relatively large values of γ obtained for both alloys are significantly higher than those predicted by conventional universality classes such as the 3D Heisenberg ($\gamma \approx 1.386$) or 3D Ising ($\gamma \approx 1.24$) models,[35] indicating that the magnetic phase transition cannot be fully described within the framework of an ideal homogeneous ferromagnet.[38,39] This anomalous behavior it is primarily associated with the intrinsic structural disorder characteristic of the amorphous state. In Fe-based amorphous alloys, the absence of long-range crystallographic order produces a broad distribution of Fe–Fe interatomic distances and local atomic environments, which in turn generates a wide distribution of exchange interaction strengths. As a consequence, the magnetic coupling becomes spatially inhomogeneous, leading to enhanced spin fluctuations and strong local variations in magnetic correlations in the vicinity of T_C.

The MAPs resulting from these critical exponents are shown in Fig. 2. Clearly, the plots exhibit the expected concavity in the low-magnetic-field region, which evolves toward a linear trend at moderate and high values of the applied magnetic field. Furthermore, the extrapolation of the isothermal plot at T_C passes through the origin, thereby confirming the proper selection of critical exponents. The temperature dependence of the spontaneous magnetization, M_s, was determined by linearly extrapolating the high-field MAPs to the y-axis intercept for $T < T_C$.[37] Similarly, the inverse of the magnetic susceptibility (χ_0^{-1}) was derived from the MAPs at $T > T_C$ (both are depicted in Fig. 3).

The $M_S(T)$ and $\chi_0^{-1}(T)$ curves for both A and B ribbons vanish at $T = T_C$ within the experimental uncertainty. A noticeable deviation from linearity in $\chi_0^{-1}(T)$ is observed in the temperature region immediately above T_C, indicating the presence of persistent short-range magnetic correlations within the paramagnetic range. This behavior is consistent with the analysis of the critical exponents.

Magnetocaloric properties of individual ribbons

The temperature dependence of the isothermal magnetic entropy change for ribbons A and B under different magnetic field values (1–8 T) is shown in Fig. S5a and b. The curves exhibit wide peaks with caret-like shape characteristic of SOMPT materials. For ribbon A, the maximum of $|\Delta S|$ reaches approximately 2.1(4) J kg^{-1} K^{-1} [1.1(2) J kg^{-1} K^{-1}] under $\mu_0\Delta H$ = 5 T [2 T] around 340 K, while for ribbon B, $|\Delta S|^{max}$ = 1.8(4) J kg^{-1} K^{-1} [0.93(19) J kg^{-1} K^{-1}] near 290 K. The width of the $\Delta S(T)$ curves for $\mu_0\Delta H$ = 2 T reaches 138 K and 128 K for the ribbons A and B, respectively. This broadening is characteristic of Fe-based metallic glasses and originates from their inherent structural disorder, which ultimately leads to the relatively wide magnetocaloric response.[40,41]

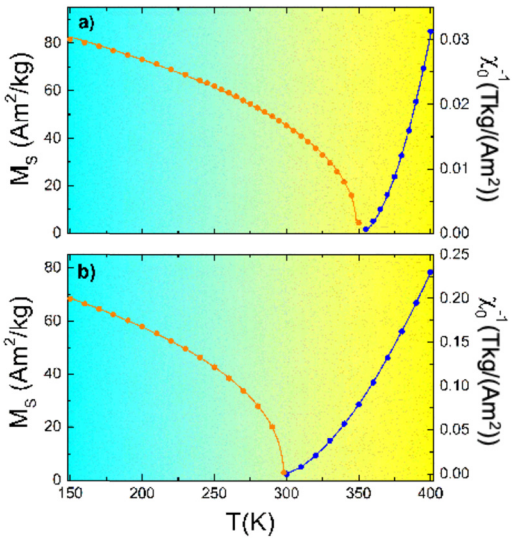

Fig. 3 Temperature dependence of the spontaneous magnetization M_S and the inverse magnetic susceptibility χ_0^{-1} for (a) ribbon A, and (b) ribbon B. The solid points are the experimental data extracted from modified Arrot plots, while the lines represent the fits to the Kouvel–Fisher equations, $M_s = M_0(1 - T/T_C)^\beta$ and $\chi_0^{-1} = \Gamma(T/T_C - 1)^\gamma$ (see text for further details).

MCE offers a powerful framework for systematically probing critical behavior by incorporating the complete temperature dependence of the isothermal entropy change. In this context, the method proposed by Franco *et al.*[42,43] provides a robust tool for determining whether different materials belong to the same universality class. This approach relies on constructing a normalized entropy change curve by (i) scaling each $|\Delta S|(T)$ dataset to $|\Delta S|^{max}$ and (ii) rescaling the temperature axis as:

$$\theta = -\frac{T - T_C}{T_r - T_C} \quad (4)$$

where T_r represents a reference temperature below T_C corresponding to $|\Delta S|/|\Delta S|^{max} = a_S$, typically taken as 0.5.[42] The rescaled $\Delta S(T)$ datasets in Fig. 4a and b collapse onto a single curve, a hallmark of a single-phase magnetic transition.[44] This scaling behavior reflects the universality class of both materials. Furthermore, the renormalized curves for both ribbons overlap, indicating that the two compositions belong to the same universality class,[43,44] as expected from the similar critical exponents β and γ.

Magnetocaloric properties of biphasic composites

After the individual characterization of ribbons A and B, we evaluated the MC response of the biphasic composites made by the two ribbons with different relative weight ratios. To this end, the isothermal magnetic entropy change of the composites was calculated by linearly combining the $\Delta S(T)$ curves of the ribbons A and B (see eqn (2)). This strategy has been previously proved to be effective in predicting the behavior of biphasic composites designed from Fe-based amorphous ribbons.[8,45]

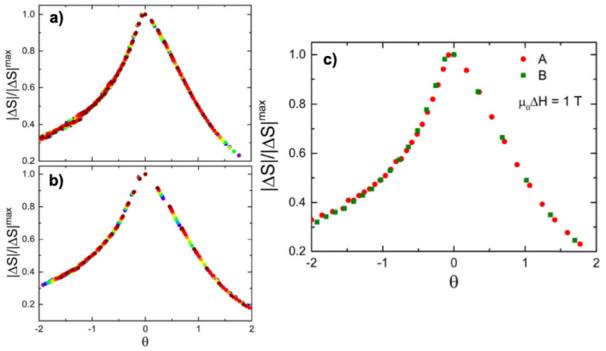

Fig. 4 Normalized magnetic entropy change curves $|\Delta S|/|\Delta S|^{max}$ as a function of the rescaled temperature θ (see eqn (4)) for (a) ribbon A, and (b) ribbon B. The collapse of all curves onto a single universal curve confirms the scaling behavior and the second-order nature of the transition. (c) Comparison of the universal curves of ribbon A (red circles) and ribbon B (green squares). The nearly identical shape of both master curves indicates that both alloys belong to the same universality class, consistent with their similar critical exponents (see text for further details).

Fig. S6 represents the temperature dependence of $|\Delta S_{comp}|$ for a weight fraction of 0.5 under $\mu_0\Delta H$ up to 8 T. Also, for the magnetic field change ($\mu_0\Delta H \leq 1$ T) a double-peak profile is still evident in the $|\Delta S_{comp}(T)|$ curves, reflecting the magnetic transitions of the individual alloys. However, upon increasing the magnetic field ($\mu_0 H \geq 1$ T), the broadening of the single $\Delta S(T)$ curves yields a more uniform superposition, ultimately leading to a flat region usually known as table-like behavior.

Fig. 5a displays the temperature dependence of $|\Delta S_{comp}(T)|$ for composites with different weight fractions (α ranging from 0 to 1) under a magnetic field change of 5 T. Due to the combination of two alloys with different values of the Curie temperature, the maximum of $|\Delta S_{comp}(T)|$ is reduced compared with the $|\Delta S|^{max}$ of the individual ribbons. In the case of the composite with $\alpha = 0.5$, $|\Delta S_{comp}|^{max} = 1.7$ J kg^{-1} K^{-1} for $\mu_0\Delta H =$ 5 T, smaller than $|\Delta S_A|^{max}$ and $|\Delta S_B|^{max}$ (see Fig. S5 and S6). Notably, a table-like shape of the curve emerges for specific weight fractions. Among the simulated composites, the most pronounced table-like behavior for $\mu_0\Delta H = 5$ T (highlighted as black line in Fig. 5a) is obtained for $\alpha = 0.5$. The resulting plateau extends approximately between T_C^A (340 K) and T_C^B (300 K). For lower or higher values of α the plateau becomes less uniform and eventually a single-peak profile appears, with the maximum shifting toward the magnetic transition temperature of the dominant phase. For example, at $\alpha = 0.8$, a well-defined peak appears near 300 K, with a narrower temperature span than in the table-like profile.

Fig. 5b shows the simulated $|\Delta S_{comp}|(T)$ curves for composites with different weight fractions under magnetic field changes of 2, 5, and 8 T. The optimum values of α evolve between 0.4 for 2 T and 0.6 for 8 T, due to the distinct magnetic field dependence of the individual $\Delta S(T)$ curves (see Fig. 5c). As

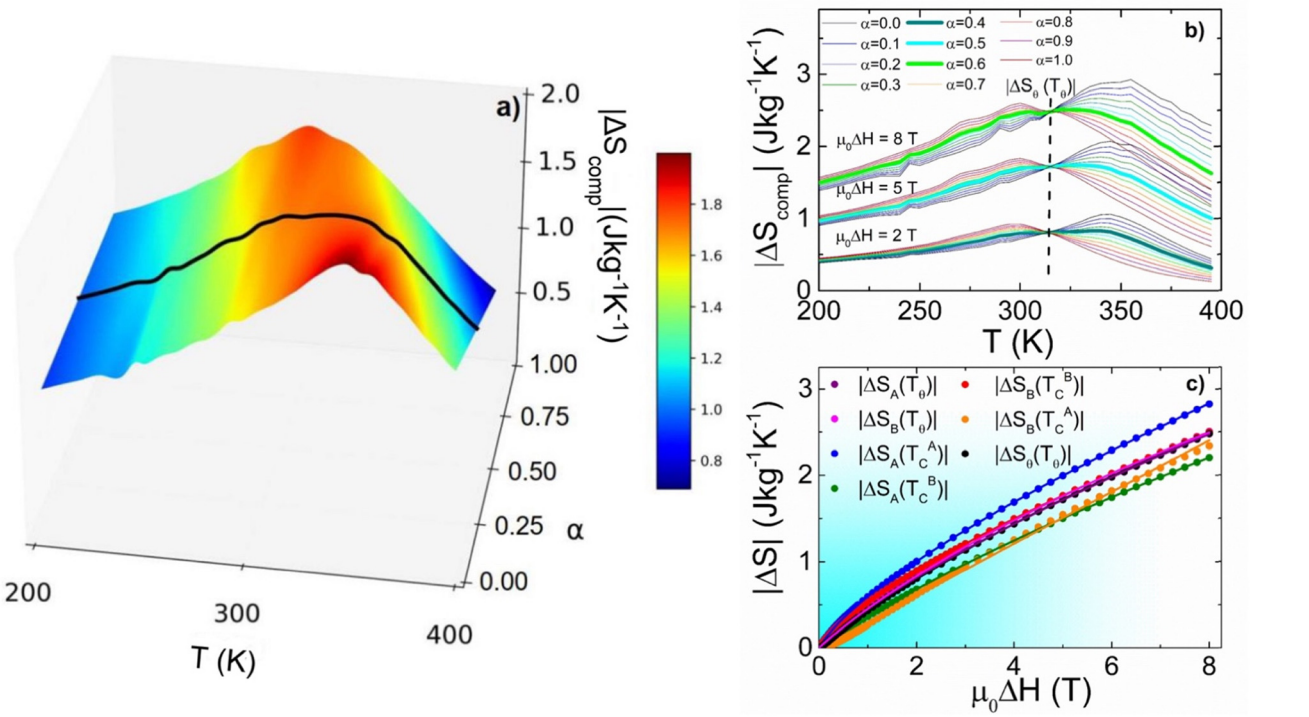

Fig. 5 (a) Isothermal magnetic entropy change of the composite (ΔS_{comp}) as a function of temperature and weight fraction A-type ribbon (α) for the biphasic composite under an applied magnetic field change of 5 T. The composite exhibits a table-like ΔS_{comp} profile over ≈50 K, delimited by the Curie temperatures of the two ribbons. (b) $|\Delta S_{comp}|(T)$ curves calculated from the $\Delta S(T)$ curves measured for A and B amorphous ribbons under $\mu_0\Delta H = 2$ T, 5 T, and 8 T. For each value of the magnetic field, the curve corresponding to the table-like variation has been highlighted. The cut-off point $|\Delta S_\theta|$ is indicated by a dashed line. (c) Applied magnetic field dependence of the magnetic entropy change for ribbons A and B for characteristic temperatures T_C^A, T_C^B, and T_θ. Lines correspond to the theoretical fits of ΔS *vs.* $\mu_0 H$ obtained from eqn (7) (see text for details).

previously noted,[45] all $|\Delta S_{comp}|(T)$ curves intersect at a common point, ΔS_θ, at T_θ for a given applied magnetic field. The ΔS_θ value provides a practical constraint for engineering table-like composites, since it limits the maximum $|\Delta S_{comp}|$ achievable in the plateau region. Notably, T_θ is found to be field-independent (T_θ = 315 K up to $\mu_0\Delta H$ = 8 T), suggesting that $\Delta S_A(T_\theta)$ and $\Delta S_B(T_\theta)$ exhibit a similar magnetic field dependence. Fig. 5c depicts the magnetic field dependence of ΔS_θ together with ΔS of the individual ribbons at T_C^A, T_C^B, and T_θ.

Interestingly, $\Delta S_A(T_\theta)$ and $\Delta S_B(T_\theta)$ remain essentially identical, as predicted above. Across the entire magnetic field range, $|\Delta S_\theta|$ exhibits lower values than $|\Delta S_A(T_C^A)|$ and $|\Delta S_B(T_C^B)|$, but higher than $|\Delta S_A(T_C^B)|$ and $|\Delta S_B(T_C^A)|$, with $|\Delta S_\theta| \approx 0.82$, 1.8 and 2.6 J kg^{-1} K^{-1} for $\mu_0\Delta H$ = 2, 5 and 8 T, respectively. Noteworthy, the magnetic-field dependence of both the individual and biphasic $|\Delta S(T)|$ curves follows a nonlinear power-law behavior, $|\Delta S| \propto \mu_0\Delta H^n$, typical of materials experiencing a SOMPT.[43]

The exponent n depends on both temperature and magnetic field in FM materials and it can be estimated as:[46]

$$n(T,H) = \frac{\partial \ln|\Delta S|}{\partial \ln \mu_0 \Delta H} \quad (5)$$

Moreover, the value of n at T_C is linked to the critical exponents β and δ governing the SOMPTs:[46]

$$n(T_C) = 1 + (1/\delta)(1 - 1/\beta) \quad (6)$$

which makes n a valuable parameter for probing the universality class of magnetic phase transitions using magnetocaloric data. For materials following an MF approach, this critical exponent is expected to be n = 2/3 at $T = T_C$.[43] In our case, the values of n obtained from the critical exponents are 0.716(7) and 0.718(5) for the ribbons A and B, respectively, close to the value given from the MF prediction and consistent with the analysis presented in the previous section.

Furthermore, we have analyzed the magnetic field dependence of the maximum of the isothermal magnetic entropy change, which can be described using Landau's theory for SOMPT as:[47,48]

$$|\Delta S|^{max} = A(H + H_0)^{2/3} - AH_0^{2/3} + BH^{4/3} \quad (7)$$

where A and B are intrinsic composition-dependent parameters, and H_0 is an extrinsic parameter that primarily reflects sample quality and microstructural effects. The isothermal magnetic entropy change depends primarily on the spontaneous magnetization (*i.e.*, related to β) and its temperature variation, while deviations in the critical susceptibility do not affect significantly the validity of the fit.[49] The lines in Fig. 5c represent the fit of the $|\Delta S|^{max}$ *vs.* $\mu_0\Delta H$ data. In this work, we restricted the analysis to the 2/3-power law. The obtained values for A and H_0 are compiled in Table 1. The intrinsic parameter A slightly varies between ribbons A and B, consistent with the similar magnetic exchange coupling expected for both samples. In contrast, the extrinsic H_0 parameter exhibits a more pronounced difference between the two ribbons. This behavior is less straightforward to interpret because H_0 is highly sensitive to microstructural imperfections. The observed larger H_0 value for ribbon B can be attributed to a higher atomic disorder. The values obtained from the fit fall within the ranges reported for other magnetic systems undergoing a SOMPT, such as the 2 : 17 alloys $Pr_{1.64}Sm_{0.36}Fe_{17}$,[50] and Tb_2Fe_{17},[51] as well as other families of compounds, including $Mn_5Ge_{3-x}Zn_x$,[52] $Gd_{1-x}Sm_xCo_2$,[53] and Ni-doped MnCoGe.[54]

To evaluate the suitability of a magnetic material for refrigeration applications, two primary figures of merit are commonly considered. The first is the refrigerant capacity (RC), that quantifies the heat absorbed from the cold reservoir and released to the hot reservoir during an Ericsson cycle of refrigeration, and can be estimated using three different criteria:[55–57] (i) RC-1, defined as the area of a rectangle with height $|\Delta S|^{max}$ and base equal to the full width at half maximum of the $|\Delta S(T)|$ curve (δT_{FWHM}); (ii) RC-2, given by the area under $|\Delta S(T)|$ within δT_{FWHM}; and (iii) RC-3, obtained *via* the Wood and Potter method, which identifies the rectangle with maximum area under the $|\Delta S(T)|$ curve. Fig. S7 schematically illustrates the procedure used to determine RC-1 and RC-2. These definitions are consistent with a reversible Ericsson cycle operating between a cold reservoir at T_{cold} and a hot reservoir at T_{hot}, in which the maximum energy that can be extracted from the cold reservoir is $T_{hot}\,|\Delta S(T_{cold})|$. Furthermore, by the second law of thermodynamics, the energy released at the hot reservoir must be equal to $T_{cold}\,|\Delta S(T_{cold})|$.

Consequently, any ΔS values exceeding $|\Delta S(T_{cold})|$ do not contribute to the refrigeration process; in other words, the peak of the $|\Delta S(T)|$ curve does not fully reflect the material thermodynamic utility. Although the definitions of RC commonly used in the literature provide a reference for comparing materials, they fail to ascertain the practical performance of systems with broad or table-like entropy changes. For such materials, a figure of merit that better denotes the practical heat transfer across the plateau is the effective refrigerant capacity, RC_{eff}, defined as:[8]

$$RC_{eff} = |\Delta S_\theta| \cdot \Delta T \quad (8)$$

Table 1 Fitted parameters A and H_0 obtained from the refinement of the experimental data shown in Fig. 5(c) using eqn (7). The reduced chi-squared (χ^2) values are also provided as a measure of the goodness of the fit. The uncertainties correspond to one standard deviation

	Composite α = 0.5	Ribbon A $T_C = T_C^A$	Ribbon A $T_C = T_C^B$	Ribbon A $T_C = T_\theta$	Ribbon B $T_C = T_C^A$	Ribbon B $T_C = T_C^B$	Ribbon B $T_C = T_\theta$
$A\,\mu_0^{-2/3}$ (J kg^{-1} K^{-1} T$^{-2/3}$)	0.758 (3)	0.756 (2)	0.7082 (8)	0.7237(9)	1.7 (4)	0.662 (2)	0.739 (4)
$\mu_0 H_0$ (T)	1.14 (3)	0.210 (7)	1.74 (1)	0.776 (8)	5 (4)	0.178 (6)	0.79 (3)
χ^2	1.23	1.07	1.06	1.06	1.36	1.06	1.17

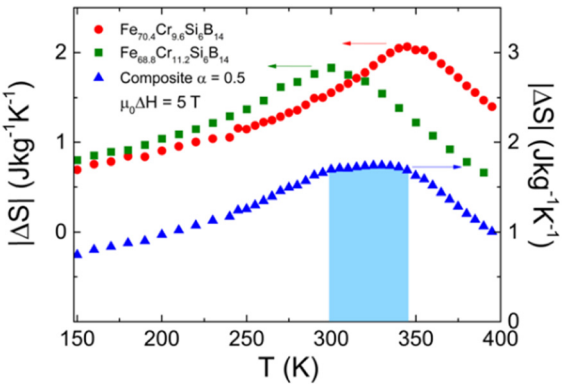

Fig. 6 Comparison of the isothermal magnetic entropy change for the individual ribbons and the composite with A-ribbon weight fraction $\alpha = 0.5$ for $\mu_0\Delta H = 5$ T. The shaded blue area highlights the table-like region.

where ΔT represents the width of the plateau and $|\Delta S_\theta|$ the value of ΔS_{comp} within the plateau (sketched in Fig. S7). Fig. 6 depicts the $|\Delta S_{comp}|(T)$ curve for the composite with $\alpha = 0.5$ under $\mu_0\Delta H = 5$ T, showing a broad plateau ($\approx$300–340 K) with $|\Delta S_\theta| \approx 1.7$ J kg^{-1} K^{-1}, which yields an RC_{eff} of 87 J kg^{-1}.

Over the same temperature interval, the composite extracts more internal energy from the cold reservoir during a refrigeration cycle than either alloy alone, by efficiently combining the contributions of both phases. Moreover, although the individual alloys exhibit higher ΔS peaks (see Fig. 6), their narrower temperature span limits the usable range in an hypothetical Ericsson cycle. In contrast, the composite provides a functional plateau between 300 K and 340 K, which aligns well with the typical operating range of conventional refrigeration systems. To place the performance of the biphasic composite with $\alpha = 0.5$ in the context of the current state of the art, data for several table-like MC materials reported in the literature are given in Table 2, with values of RC_{eff} as a function of the central temperature (T^*) under 2 and 5 T applied magnetic field values.

It is worth noting that rare-earth-based composites generally exhibit higher RC_{eff} due to their larger isothermal magnetic entropy change peak values. However, these systems typically operate at cryogenic temperatures or require critical raw materials. In contrast, the Fe-based composite presented here operates near RT and offers a notably broad temperature span ($\Delta T_{table} \approx$ 50 K). The obtained RC_{eff} value of 87 J kg^{-1} at 5 T is competitive among rare-earth free materials, surpassing other Fe-based metallic glasses and thin films. Under an applied magnetic field of 2 T, the magnetic entropy change reaches 0.8 J kg^{-1} K^{-1}. Nevertheless, the broad operational temperature span ($\sim$50 K) results in an RC_{eff} of 37.5 J kg^{-1}, which is among the highest values reported for rare-earth-free compositions operating near RT.

The second figure of merit derives from the critical assessment conducted by Griffith *et al.*,[58] which underscores the inherent complexity of magnetocaloric materials. It emphasizes that reducing their performance to a single figure of merit inevitably leads to oversimplification. Consequently, meaningful comparisons must consider temperature and magnetic field-dependent properties, hysteresis effects, and practical factors such as thermal conductivity, corrosion resistance, and mechanical stability.

Within this framework, the temperature-averaged entropy change has emerged as a complementary metric for material screening and for comparing performance across different caloric families (magnetocaloric, electrocaloric, and elastocaloric) over application-relevant temperature spans.[59–61] Our results for Fe–Cr–Si–B amorphous composites are consistent with this perspective. Our work prioritizes achieving a broad, table-like ΔS profile over approximately 50 K. Furthermore, the SOMPT characteristic of these amorphous alloys ensure intrinsically low thermal and magnetic hysteresis, thereby avoiding the cyclability issues that often complicate the interpretation of TEC in first-order systems (Fig. 7).

TEC is therefore proposed as a simple, material-based figure of merit and is defined as:[58]

$$\mathrm{TEC}(\Delta T_{lift}) = \frac{1}{\Delta T_{lift}} \max_{T_{mid}} \int_{T_{mid}-\frac{\Delta T_{lift}}{2}}^{T_{mid}+\frac{\Delta T_{lift}}{2}} -\Delta S(T)_{\Delta H,T} \mathrm{d}T \qquad (9)$$

where ΔT_{lift} and T_{mid} denote the width and midpoint of the temperature interval over which the integral is evaluated,

Table 2 Comparison of magnetocaloric parameters for various composites reported in the literature and for the current Fe–Cr–Si–B composite with weight fraction $\alpha = 0.5$, measured under magnetic field changes of 2 and/or 5 T as indicated. The listed quantities are: the application temperature T^*, the table-like temperature range ΔT_{table}, the isothermal entropy change of the composite ΔS_{comp}, and the effective refrigerant capacity RC_{eff}. Where available, values for both field changes are provided

Family of alloys	$\mu_0 H$ (T)	T^* (K)	ΔT_{table} (K)	$\lvert\Delta S_{comp}\rvert$ (J kg^{-1} K^{-1})	RC_{eff} (J kg^{-1})	Ref.
$Fe_{(80-x)}Cr_xSi_6B_{14}$	2/5	315	50/50	0.8/1.7	37.5/87	This work
$Fe_{87}La_{(7-x)}Ce_5Co_1$	1.5/5	310	58/58	1.5/3.1	85/181	62
$Fe_{(88-x)}Nd_xCr_8B_4$	2/5	335	40/40	1.5/3.2	60/128	63
$Fe_{(78-x)}Ce_xSi_4Nb_5B_{12}Cu_1$	—/5	310	—/40	—/2.1	40/84	64
$Fe_{(88-x)}Co_xZr_8B_4$	—/5	305	—/20	—/3.0	25/60	65
$La_{(1-x)}Pr_xFe_{10.7}Co_{0.8}Si_{1.5}$	2/5	285	10/10	5/7.5	30/75	66
$(La_{0.6}Ba_{0.2}Sr_{0.2}MnO_3)_{1-x}/(Co_2O_3)_x$	2/4.5	320	40/40	1/2.0	40/80	67
$La_{2/3}Ba_{1/3}MnO_{(3-x)}$	1/–	325	35/–	1.3/–	46/–	68
$Gd_{50}Co_{48}(Fe,Mn)_2$	2/5	250	40/40	1.7/4.3	85/172	69
Ho_5Pd_2/Ho_3Pd_2	2/5	25	19/25	3/10	—/429	16
$(Er_2Cr_2C_3)_x/(Ho_2Cr_2C_3)_{(1-x)}$	2/–	10	15/–	6/–	60/–	70
$ErZn_2/ErZn$	2/5	12	10/10	8/16	96/232	71
$Fe_{87}Pr_{10-x}B_3Ce_x$	—/5	316	—/30	—/3.8	—/114.9	72

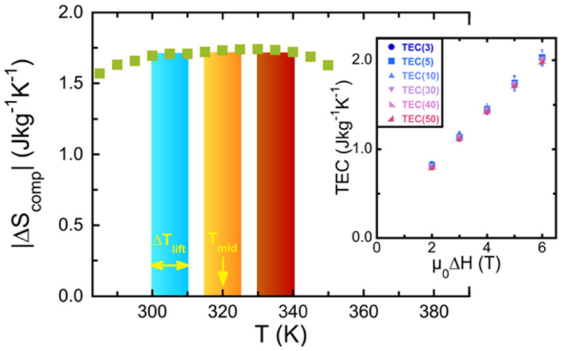

Fig. 7 Temperature dependence of $|\Delta S_{comp}|$ measured under $\mu_0\Delta H$ = 5 T. Shaded rectangles illustrate the different regions around the midpoint temperature (T_{mid}) with the same temperature span (ΔT_{lift}) used for determining TEC (see eqn 9). The height of each region corresponds to the nearly constant table-like value of $|\Delta S_{comp}|$ within the selected interval. Inset: TEC of the composite with α = 0.5 as a function of the applied magnetic field for selected ΔT_{lift} values within the magnetic-field range where the table-like MCE behavior is preserved. The procedure for calculating error bars is detailed in the SI.

respectively. In essence, TEC provides the maximum average entropy change within all temperature intervals of width ΔT_{lift}. Fig. 7 and its inset reveal that the TEC in the table-like region exhibits no appreciable dependence on T_{mid} and ΔT_{lift}.

These observations underscore that in Fe-based amorphous composites exhibiting a table-like MCE, TEC remains essentially independent of the operating temperature range, providing reliable and versatile performance for Ericsson-cycle magnetic refrigeration processes. This makes such composites especially advantageous for practical RT applications, where stable and field-independent performance is critical. Consequently, this material provides a suitable compromise between performance, operational range, and cost, reinforcing the suitability of Fe-based amorphous alloys for domestic refrigeration applications.

The wide table-like magnetocaloric effect originates from the dual-phase amorphous structure. Specifically, when two amorphous phases are combined with an appropriate fraction ratio and a suitable difference in their Curie temperatures (owing to different Fe–Fe distances and exchange coupling interactions), the working temperature span is significantly broadened. This effect, together with the comparable magnetic entropy changes of the individual phases, results in a high overall magnetocaloric response.

Conclusions

The magnetic critical behavior and magnetocaloric performance of $Fe_{70.4}Cr_{9.6}Si_6B_{14}$ and $Fe_{68.8}Cr_{11.2}Si_6B_{14}$ amorphous ribbons have been systematically investigated. Both alloys exhibit a second-order magnetic phase transition, with critical exponents that deviate from the conventional mean-field predictions and instead reflect a coexistence of long- and short-range magnetic interactions, consistent with an intermediate universality class. The close correspondence between the exponent sets for both compositions demonstrates that they indeed share the same universality class, a conclusion further reinforced by the trend followed by their magnetocaloric behavior. The ribbons achieve maximum isothermal magnetic entropy changes of 2.1 J kg^{-1} K^{-1} (1.1 J kg^{-1} K^{-1}) and 1.8 J kg^{-1} K^{-1} (0.93 J kg^{-1} K^{-1}), respectively, under a change of the applied magnetic field of 5 T (2 T) underscoring the intrinsic efficiency of these amorphous systems.

For evaluating materials intended for Ericsson-cycle refrigeration, where a broad and nearly constant ΔS response is preferred over a sharp magnetic entropy change peak, RC_{eff} and TEC are particularly relevant figures of merit. Building on the findings obtained for the Fe–Cr–Si–B amorphous ribbons, the optimally designed and engineered composite that integrates both amorphous ribbons delivers a broad table-like ΔS profile with a nearly constant magnitude of $\Delta S \approx 1.7$ J kg^{-1} K^{-1} under an applied magnetic field change of 5 T across a temperature span of about 50 K. This behavior results in a highly competitive RC_{eff} among rare-earth-free materials operating near room temperature and a TEC that remains nearly independent of ΔT_{lift}. In addition, the SOMPT of these amorphous alloys minimizes hysteresis effects, which is advantageous for cyclic operation. Crucially, this performance achieved in low-magnetic-loss Fe-based amorphous systems without reliance on critical raw chemical elements establishes Fe–Cr–Si–B metallic glasses and their composites not merely as model systems for probing magnetic phase transitions, but as genuinely viable candidates for scalable, sustainable, next-generation magnetocaloric refrigeration technologies.

Author contributions

A. S.-P.: data curation, formal analysis, visualization, writing original draft; J. L.-G.: formal analysis, validation, visualization, writing original draft.; K. P.-A.: visualization, data curation; J.-M. P.: formal analysis, visualization, funding acquisition; J.-L. S.: investigation; J.-A. B.: formal analysis, validation, visualization, writing final version; P. G. conceptualization, supervision, writing final version. P. A.-A.: conceptualization, data curation, investigation, funding acquisition, methodology, project administration, software, visualization, writing original draft. All authors participated in the writing, review and editing of the final version of the manuscript.

Conflicts of interest

The authors declare that there are no conflicts to declare.

Data availability

The raw data supporting the findings of this study, including magnetization isotherms, critical exponent analysis, and entropy change calculations, are available from the corresponding author upon reasonable request. Processed data and the analysis scripts used for the calculation of ΔS, RC_{eff}, and

TEC have been deposited in https://zenodo.org/communities/magcoolest/. Supplementary information (SI) is available. See DOI: https://doi.org/10.1039/d6ma00481d.

Acknowledgements

This work was financially supported by SEK-25-GRU-GIC-24-113 from SEKUENS, Principality of Asturias and the Spanish MCIN/AEI/10.13039/501100011033 and ERDF, EU PID2022-138256NB-C21 and PID2022-138256NA-C22. A. S.-P. acknowledges funding received through the Avenir 2025/2026 fellowship awarded by the Embassy of France in Spain. J.-M. P. acknowledges the Ramón y Cajal grant RYC2023–044841-I funded by MICIU/AEI/10.13039/501100011033. J. L. S. L. ackowledges the support received from Laboratorio Nacional de Nanociencias y Nanotecnología (LINAN, IPICyT) and M.Sc. Beatriz Rivera Escoto for her technical support.

Notes and references

1 Y. Liao, H. Sha, C. M. O'Leary, H. Zhong, Y. Yang and J. Miao, *Nature*, 2026, **649**, 1123.
2 S. Yamaura, W. Zhang, R. Y. Umetsu, G. Xie and I. Seki, Applications of Amorphous Alloy/Metallic Glass for Environmental and Energy Engineering, Electronics Engineering, and Biomedical Engineering Fields, in *Novel Structured Metallic and Inorganic Materials*, ed Y. Setsuhara, T. Kamiya and S. Yamaura, Springer, Singapore, 2019, ch. 2.
3 A. Vinod, D. A. Babu, M. R. Muthuvel, P. Ramasamy and W. Madhuri, *J. Mater. Chem. C*, 2025, **13**, 8228.
4 M. S. Reis, *Coord. Chem. Rev.*, 2020, **417**, 213357.
5 P. Z. Z. Nehan, O. Vitayaya, D. R. Munazat, M. T. E. Manawan, D. Darminto and B. Kurniawan, *Phys. Chem. Chem. Phys.*, 2024, **26**, 14476.
6 J. Zhou, J. You and K. Qiu, *J. Appl. Phys.*, 2026, **132**, 040702.
7 V. Franco, J. S. Blázquez, J. J. Ipus, J. Y. Law, L. M. Moreno-Ramírez and A. Conde, *Prog. Mater. Sci.*, 2018, **93**, 112.
8 P. Álvarez, J. Sánchez Marcos, P. Gorria, L. Fernández Barquín and J. A. Blanco, *J. Alloys Compd.*, 2010, **504**, S150.
9 P. Álvarez, P. Gorria, J. Sánchez Marcos, L. Fernández Barquín and J. A. Blanco, *Intermetallics*, 2010, **18**, 2464.
10 V. Franco, J. S. Blázquez, B. Ingale and A. Conde, *Annu. Rev. Mater. Res.*, 2012, **42**, 305.
11 A. Smaïli and R. Chahine, *J. Appl. Phys.*, 1997, **81**, 824.
12 P. Álvarez, P. Gorria, J. L. Sánchez Llamazares and J. A. Blanco, *J. Alloys Compd.*, 2013, **568**, 98.
13 R. M'nassri, *Eur. Phys. J. Plus*, 2016, **131**, 392.
14 W. Akram, M. de h-Óra, M. Bansal, R. Mukhopadhyay, J. MacManus-Driscoll and T. Maity, *J. Phys. D: Appl. Phys.*, 2023, **57**, 055301.
15 M. Guel-Rodríguez, J. Zamora, C. F. Sánchez-Valdés, J. L. Sánchez Llamazares and P. Álvarez-Alonso, *J. Alloys Compd.*, 2024, **978**, 173452.
16 X. Wu, Y. Du, X. Gao, F. Liu, L. Ma, G. Cheng, J. Wang, J. Zhao and G. Rao, *J. Alloys Compd.*, 2025, **1010**, 177742.
17 S. Chefi, M. M. Nofal, E. M. A. Dannoun and R. M'nassri, *Emerg. Mater.*, 2025, **8**, 741.
18 S. Shao, G. Wang, H. Yin, X. Jin, M. Gao, L. Song, W. Xu, G. Wang, J. Q. Wang and J. Huo, *Mater. Today Commun.*, 2026, **52**, 115060.
19 H. Nam, J. Lee, S. Kim, I. Sohn, K. Yun, C. Jung and S. Yi, *Materialia*, 2025, **44**, 102588.
20 S. Zhang, D. Ma, P. Shen, B. Sun, H. Chen and Z. Zhang, *China Foundry*, 2025, **22**, 427.
21 A. Inoue, A. Takeuchi and B. Shen, *Mater. Trans.*, 2001, **42**, 970.
22 A. El Boubekri, M. Ounacer, M. Sajieddine, M. Sahlaoui, H. Lassri, A. Essoumhi, E. K. Hlil, A. Razouk and E. Agouriane, *Phys. B*, 2023, **663**, 414997.
23 A. El Boubekri, S. Tillaoui, A. Razouk, M. Sahlaoui, H. Lassri, E. K. Hlil and M. Sajieddine, *Curr. Appl. Phys.*, 2024, **59**, 60.
24 A. El Boubekri, S. Tillaoui, M. Sajieddine, M. Sahlaoui, H. Lassri, E. K. Hlil, E. Agouriane and A. Razouk, *J. Magn. Magn. Mater.*, 2020, **507**, 166819.
25 P. Álvarez-Alonso, J. D. Santos, M. J. Pérez, C. F. Sánchez-Valdes, J. L. Sánchez Llamazares and P. Gorria, *J. Magn. Magn. Mater.*, 2013, **347**, 75.
26 V. K. Pecharsky, K. A. Gschneidner and A. M. Tishin, *Phys. Rev. B: Condens. Matter Mater. Phys.*, 2001, **64**, 1444061.
27 A. Smatli and R. Chahine, *Adv. Cryog. Eng.*, 1996, **42**, 445.
28 A. T. Aldred, B. D. Rainford, J. S. Kouvel and T. J. Hicks, *Phys. Rev. B*, 1976, **14**, 228.
29 J. M. D. Coey, *Magnetism and Magnetic Materials*, Cambridge University Press, Cambridge, 2010, vol. 1.
30 B. K. Banerjee, *Phys. Lett.*, 1964, **12**, 16.
31 A. Arrot, *Phys. Rev.*, 1957, **108**, 1394.
32 A. Arrott and J. E. Noakes, *Phys. Rev. Lett.*, 1967, **19**, 786.
33 S. N. Kaul, *J. Magn. Magn. Mater.*, 1985, **53**, 5.
34 B. Widow, *J. Chem. Phys.*, 1965, **43**, 3898.
35 M. Sambasiva Rao and S. N. Kaul, *J. Magn. Magn. Mater.*, 1995, **147**, 149.
36 S. F. Fischer, S. N. Kaul and H. Kronmüller, *Phys. Rev. B: Condens. Matter Mater. Phys.*, 2002, **65**, 644431.
37 S. N. Kaul, *Phys. Rev. B: Condens. Matter Mater. Phys.*, 1980, **22**, 278.
38 C. M. Haetinger, L. Ghivelder, J. Schaf and P. Pureur, *J. Phys.: Condens. Matter*, 2009, **21**, 506006.
39 A. El Boubekri, S. Tillaoui, A. Razouk, M. Sahlaoui, H. Lassri, E. K. Hlil and M. Sajieddine, *Curr. Appl. Phys.*, 2024, **59**, 60.
40 P. Alvarez-Alonso, J. L. Sánchez Llamazares, C. F. Sánchez-Valdés, G. J. Cuello, V. Franco, P. Gorria and J. A. Blanco, *J. Appl. Phys.*, 2014, **115**, 17A929.
41 A. Firlus, M. Stoica, J. Wright, X. Sun, R. E. Schäublin and J. F. Löffler, *J. Alloys Compd.*, 2025, **10**, 180013.
42 V. Franco, A. Conde, J. M. Romero-Enrique and J. S. Blázquez, *J. Phys.: Condens. Matter*, 2008, **20**, 285207.
43 V. Franco and A. Conde, *Int. J. Refrig.*, 2010, **33**, 465.
44 C. M. Bonilla, J. Herrero-Albillos, F. Bartolomé, L. M. García, M. Parra-Borderías and V. Franco, *Phys. Rev. B: Condens. Matter Mater. Phys.*, 2010, **81**, 224424.

45 P. Álvarez, J. L. Sánchez Llamazares, P. Gorria and J. A. Blanco, *Appl. Phys. Lett.*, 2011, **99**, 232501.
46 V. Franco, J. S. Blázquez and A. Conde, *Appl. Phys. Lett.*, 2006, **89**, 222512.
47 J. Lyubina, M. D. Kuz'Min, K. Nenkov, O. Gutfleisch, M. Richter, D. L. Schlagel, T. A. Lograsso and K. A. Gschneidner Jr., *Phys. Rev. B: Condens. Matter Mater. Phys.*, 2011, **83**, 012403.
48 P. Álvarez, P. Gorria and J. A. Blanco, *Phys. Rev. B: Condens. Matter Mater. Phys.*, 2011, **84**, 024412.
49 M. Jeddi, H. Gharsallah, M. Bejar, M. Bekri, E. Dhahri and E. K. Hlil, *RSC Adv.*, 2018, **8**, 9430.
50 H. Jaballah, W. Bouzidi, R. Fersi, N. Mliki and L. Bessais, *J. Phys. Chem. Solids*, 2022, **161**, 110438.
51 J. L. Garrido-Álvarez, J. L. Sánchez Llamazares, P. Gorria and P. Álvarez-Alonso, *J. Solid State Chem.*, 2025, **350**, 125511.
52 H. Jin, Z. Liu, Y. Liu, T. Liu, J. Wang, X. Si, J. Lin and Y. Liu, *Phys. Lett. A*, 2023, **474**, 128819.
53 S. Bellafkih, H. Jaballah and L. Bessais, *J. Phys. Chem. Solids*, 2023, **178**, 111355.
54 S. Sakthivel, A. Kumar, R. Uralath Dhanavardhanan, A. Sunitha Raveendran, A. Dzubinska, M. Reiffers and N. Ramamoorthi, *Appl. Phys. A: Mater. Sci. Process.*, 2023, **129**, 428.
55 M. E. Wood and W. H. Potter, *Cryogenics*, 1985, **25**, 667.
56 K. A. Gschneidner, V. K. Pecharsky, A. O. Pecharsky and C. B. Zimm, *Mater. Sci. Forum*, 1999, **315–317**, 69.
57 P. Gorria, J. L. Sánchez Llamazares, P. Álvarez, M. J. Pérez, J. Sánchez Marcos and J. A. Blanco, *J. Phys. D: Appl. Phys.*, 2008, **41**, 192003.
58 L. D. Griffith, Y. Mudryk, J. Slaughter and V. K. Pecharsky, *J. Appl. Phys.*, 2018, **123**, 034902.
59 L. Wei, X. Zhang, J. Liu and L. Geng, *AIP Adv.*, 2018, **8**, 055312.
60 A. Biswas, T. Del Rose, Y. Mudryk, P. O. Ribeir, B. P. Alho, V. S. R. de Sousa, E. P. Nóbrega, P. J. von Ranke and V. K. Pecharsky, *J. Alloys Compd.*, 2022, **897**, 163186.
61 E. M. A. Dannoun, R. M'nassri and M. M. Nofal, *J. Mater. Sci.: Mater. Electron.*, 2025, **36**, 517.
62 Q. Wang, D. Ding, B. Z. Tang, P. Yu, J. L. Yao and L. Xia, *J. Phys. Chem. Solids*, 2022, **169**, 110854.
63 J. W. Lai, Z. G. Zheng, X. C. Zhong, V. Franco, R. Montemayor, Z. W. Liu and D. C. Zeng, *J. Magn. Magn. Mater.*, 2015, **390**, 87.
64 H. C. Tian, X. C. Zhong, Z. L. Liu, Z. G. Zheng and J. Min, *J. Non-Cryst. Solids*, 2015, **138**, 64.
65 L. Gan, L. Ma, B. Tang, D. Ding and L. Xia, *Sci. China: Phys., Mech. Astron.*, 2017, **60**, 076121.
66 R. M'nassri, *J. Supercond. Nov. Magn.*, 2016, **29**, 207.
67 R. M'nassri, N. C. Boudjada and A. Cheikhrouhou, *Ceram. Int.*, 2016, **42**, 7447.
68 R. M'nassri, *J. Supercond. Nov. Magn.*, 2016, **29**, 1879.
69 L. Y. Ma, L. H. Gan, K. C. Chan, D. Ding and L. Xia, *J. Alloys Compd.*, 2017, **723**, 197.
70 Y. Zhang, S. Li, L. Hu, X. Wuang, L. Li and M. Yan, *Mater. Today Phys.*, 2022, **27**, 100786.
71 L. Li, Y. Yuan, Y. Qi, Q. Wang and S. Zhou, *Mater. Res. Lett.*, 2018, **6**, 67.
72 Q. Wuang, D. Ding, B. Tang, R. Sun, M. Jiang and L. Xia, *J. Appl. Phys.*, 2026, **139**, 015108.